Eur. Phys. J. B **52**, 531–546 (2006)
DOI: 10.1140/epjb/e2006-00328-1

The European Physical Journal B

Extended morphometric analysis of neuronal cells with Minkowski valuations

C. Beisbart[1,2,a], M.S. Barbosa[3], H. Wagner[2], and L. da F. Costa[3]

[1] Faculty 14, University of Dortmund, 44221 Dortmund, Germany
[2] Arnold Sommerfeld Center for Theoretical Physics, Ludwig-Maximilians-Universität, Theresienstraße 37, 80333 München, Germany
[3] Cybernetic Vision Research Group, DFI-IFSC, Universidade de São Paulo, São Carlos, SP Caixa Postal 369, 13560-970, Brazil

Received 27 July 2005 / Received in final form 11 July 2006

Abstract. Minkowski valuations provide a systematic framework for quantifying different aspects of morphology. In this paper we apply vector- and tensor-valued Minkowski valuations to neuronal cells from the cat's retina in order to describe their morphological structure in a comprehensive way. We introduce the framework of Minkowski valuations, discuss their implementation for neuronal cells and show how they can be used to characterize cells of different morphological categories. We also provide a comparison to a Sholl analysis.

PACS. 07.05.Kf Data analysis: algorithms and implementation; data management – 87.19.La Neuroscience – 02.40.Ft Convex sets and geometric inequalities

1 Introduction

Natural phenomena can be understood as causes and consequences of a permanent interplay between geometry and dynamics, or form and function [1,2]. The geometric characteristics of natural objects, their distribution in space, as well as the dimensionality of space constrain their dynamics and function. For instance, the proper operation of a mammal's heart depends on a suitable diffusion of potentials and waves across the heart surface.

It is at the central nervous system that the interplay between form and function becomes most complex. For instance, the velocity of signal transmission in neuronal fibers (i.e. dendrites and axons) depends on the width and length of the fibers. Another example is as follows: neurons are cells specialized to establish selective spatial connections. Given the constraints imposed by three-dimensional space, they have to resort to the most diverse geometries in order to form the required interconnections. They do so in a dynamical way during the whole lifetime of an individual.

As a consequence, morphological analyses of neuronal cells very probably provide clues for understanding neural dynamics and function. Although a large number of investigations have been directed at the neural anatomy and geometry (e.g. [3–6]), so far only the taxonomy of neuronal cells and shape abnormalities as subsidiary for diagnosis have been investigated in depth. The study of the shape of neuronal cells with objective and mathematically well characterized morphometric descriptors is just at its beginning (e.g. [7–10]).

In order to be useful tools, morphometric descriptors should fulfill the following criteria: first, the extracted quantitative features should obey simple transformation rules, when the neuronal cell under investigation is subject to elementary geometric transformations such as affine or conformal transformations (*in-* and *covariance*). Second, the obtained measurements should discriminate between different classes of neuronal cells. Finally, it is important that the estimated features allow for intuitive interpretations from the neuroscience point of view.

Because of their long tradition in modeling and image analysis, mathematics, physics and engineering provide a large number of concepts and measures that suggest themselves for studies in neuroscience and neuromorphometry. A good example is entropy, which has been used in neuroscience because of its close association with the concept of information [11]. Other such measures include the fractal dimension [12–14], lacunarity [15,16], percolation critical density [2] and curvature [17]. Recently, concepts from Integral Geometry and the (scalar) Minkowski shape functionals, in particular, were employed to characterize the geometry of ganglion cells from the cat's retina [18,19]. For two-dimensional data, the Minkowski shape functionals comprise the volume, the area and the Euler characteristic (see below for more information). They are particularly interesting because they meet the criteria mentioned above: they are invariant under rigid body transformations, seem

---

[a] e-mail: `claus.beisbart@physik.uni-muenchen.de`

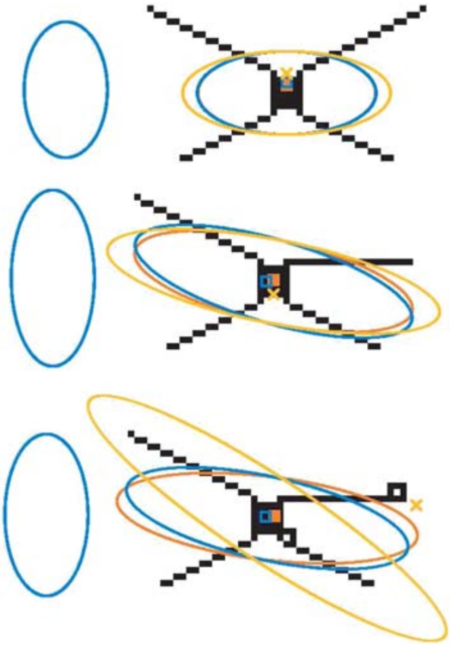

Fig. 1. Three toy examples with their curvature centroids (points) and ellipses visualizing the second-rank tensors. Point styles: red filled square: $\mathbf{p}_0$; blue open square: $\mathbf{p}_1$; yellow cross: $\mathbf{p}_2$. The ellipses carry information on the Minkowski tensors; for more information see the main text. Ellipse at the left hand side: $V_1^{0,2}$; red (medium grey) ellipse: $V_0^{2,0}$; blue (dark grey) ellipse: $V_1^{2,0}$; yellow (light grey) ellipse: $V_2^{2,0}$.

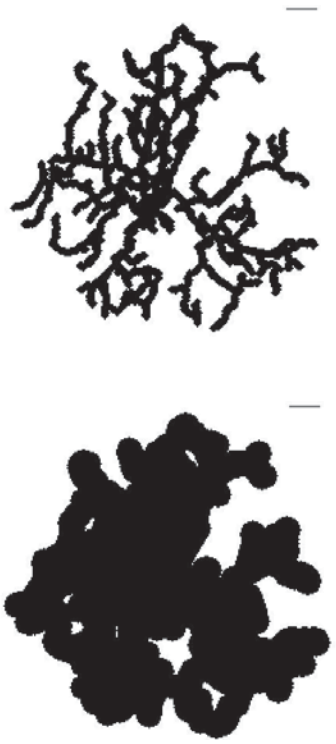

Fig. 2. Two dilations of the λ-neuron. Top panel: dilation scale $r_s = 2$ pixels. Bottom panel: $r_s = 8$ pixels. The pictures are based on data obtained by [27] (their figure No. 5, copyright permission by Nature Neuroscience).

to have good discriminative power [18], and can be squared with basic concepts from neuroscience. Moreover, they can easily be implemented: usually, the original data are filtered with methods known from MIA (Morphological Image Analysis, see below for the details of our method; for an introduction into MIA consult [20]). This preprocessing introduces a free parameter, which can later be varied in order to probe the morphology at different scales. In previous works, the singular points (branching and terminating points) [19] or the whole cell outline [18] are dilated (blown up, see [20], Ch. 3), where the dilation scale enters as a parameter. For each dilation scale, the preprocessed neuron image is decomposed into components (call them basic building blocks). The Minkowski functionals can then be calculated by counting certain multiplicities of the basic building blocks. This approach makes use of mathematical results from Integral Geometry [21].

In this paper, we use extensions of the Minkowski shape functionals, viz. the higher-rank *Minkowski valuations*, in order to further improve neuromorphometric characterization and analysis. These extensions were only recently investigated by mathematicians [22–24] and include vector- and tensor-valued measures. They are therefore sensitive to directional information and also allow for valuable graphical visualizations. Minkowski valuations have already been successfully employed to describe the morphology of galaxies [25] and galaxy clusters [26].

In the following, we will illustrate the potential of Minkowski valuations for neuromorphometry by analyzing a set of ten ganglion cells from the cat's retina. We consider two-dimensional projections of the cells. The set used [27] includes cells with diverse shapes and of different types, according to a recently revised classification of those types of cells [28]. In addition, ganglion cells from the retina exhibit branching patterns which are predominantly planar, and therefore compatible with the two-dimensional Minkowski valuations considered in the present work.

The article starts by presenting the higher-rank Minkowski valuations (Sect. 2) and proceeds by describing their application to neuronal cells (Sect. 3). Results are presented in Section 4. We draw our conclusions in Section 5.

2 Minkowski valuations

Morphometry deals with measures for the content, shape and connectivity of spatial patterns ("bodies"). Consider a body P in 2-dimensional space such as constituted by the pixels of a neuron image (see Figs. 1 and 2 for examples). A straightforward way to measure its "content" is to calculate its area $V_0(P)$ or — equivalently — to count its pixels. The area has a number of useful properties. First, it clearly meets the requirement of motion invariance as stated in the introduction. Second, it is additive; that is, the area of the set union P of two bodies P_1, P_2 can be decomposed into $V_0(P) = V_0(P_1) + V_0(P_2) - V_0(P_1 \cup P_2)$. As a consequence, the area can always be calculated by summing up over local contributions from basic building blocks (pixels, e.g.). Third, the area of a convex body can be continuously approximated by the areas of a sequence of convex polygons (conditional continuity of V_0).

There are other geometric descriptors that share these properties with the area V_0, such as the perimeter. But the class of motion-invariant, additive and conditionally continuous descriptors is not unbounded. Let us point this out in full generality for d dimensions. Consider an arbitrary pattern P that can be decomposed into a set union of finitely many convex bodies. According to *Hadwiger's characterization theorem* [29,30] there are only $(d+1)$ linearly independent measures $V_0(P)$, ..., $V_{d+1}(P)$ that obey motion-invariance, additivity and conditional continuity. They are called *(scalar) Minkowski functionals.* Thus, in our case of $d = 2$, three functionals, viz. the area V_0, the perimeter $4V_1$ and the Euler characteristic V_2 constitute a *complete* family of scalar morphological measures in the sense of Hadwiger's theorem. The Euler characteristic is a topological invariant and equals the number of connected components minus the number of holes for patterns in $\mathbb{R}^2$. The Minkowski functionals were for the first time applied to neuronal cells in [18,19].

Like the area V_0, the perimeter $4V_1$ and the Euler characteristic V_2 can be decomposed into local contributions. This time they arise from the boundary ∂P of the body P. For smooth boundaries, one has

$$V_1 = \frac{1}{4}\int_{\partial P} \mathrm{d}^1 S, \quad V_2 = \frac{1}{2\pi}\int_{\partial P} c\, \mathrm{d}^1 S, \qquad (2.1)$$

where c denotes the curvature of ∂P and varies as one moves along ∂P. For pixel sets, which do not have a smooth boundary, V_1 and V_2 can be calculated by summing up contributions from the bonds that confine the pixels, and the corners, see [21].

A natural way to generalize the concept of the Minkowski functionals is to upgrade to higher-rank Minkowski valuations, which are motion *co*variant instead of motion invariant. Motion covariance means that the Minkowski valuations obey simple transformation rules, when the body P is moved in space. Very roughly, they transform like the position vector of P or its inertia tensor with respect to some origin that is not moved with P, see [22] for details.

Motion-*co*variant, additive and conditionally continuous descriptors are called *Minkowski valuations* (MVs, for short). The class of MVs can be completely characterized by a generalization of Hadwiger's theorem [22,31]. Since motion invariance is a special case of motion covariance, the Minkowski functionals form part of the MVs. The other MVs are higher-rank moments of the Minkowski functionals.

In two dimensions there are three *first*-order moments of the Minkowski functionals, the so-called *Minkowski vectors.* For bodies with a smooth boundary, they can be represented as follows:

$$\mathbf{V}_0 = \int_P \mathbf{x}\, \mathrm{d}^2 A, \quad \mathbf{V}_1 = \frac{1}{4}\int_{\partial P} \mathbf{x}\, \mathrm{d}^1 S$$
$$\mathbf{V}_2 = \frac{1}{2\pi}\int_{\partial P} c\, \mathbf{x}\, \mathrm{d}^1 S, \qquad (2.2)$$

where $\mathbf{x}$ denotes the position vector of the area (perimeter) element $\mathrm{d}^2 A$ ($\mathrm{d}^1 S$) to be integrated over. Minkowski vectors can also be defined for pixelized images, which lack a smooth boundary.

For the purposes of our analysis, it will be useful to normalize the Minkowski vectors and to consider the *centroids*:

$$\mathbf{p}_i = \mathbf{V}_i / V_i \quad (i = 0, 1, 2 \quad \text{if} \quad V_i \neq 0). \qquad (2.3)$$

The centroids specify where some aspect of the geometry (area, perimeter, curvature) is concentrated. Note, that the centroids $\mathbf{p}_i$ may, but need not coincide with each other. It can be shown that all centroids coincide for spherically symmetric bodies.

Moving to *second*-order moments yields the *second-rank Minkowski tensors.* They are built upon the symmetric tensor product denoted by $\mathbf{x} \otimes \mathbf{x} =: \mathbf{xx} =: \mathbf{x}^2$. In two dimensions there are more than three tensors, because, for ∂P-integrals, instead of calculating moments with respect to the spatial position $\mathbf{x}$, one can also consider the local normal $\mathbf{n}$ of the boundary, which points outwards and is normalized to one[1]. Thus, for the integrals $\int_{\partial P} \mathrm{d}^1 S$ and $\int_{\partial P} c \mathrm{d}^1 S$, three types of second-order weights for building moments are available, namely $\mathbf{x}^r \mathbf{n}^s$, where $(r, s) = (2, 0)$, $(1, 1)$ and $(0, 2)$ (since we only consider symmetric moments, $\mathbf{nx}$ and $\mathbf{xn}$ are identical). Altogether the following seven tensors can be formed:

$$V_0^{2,0} = \int_P \mathbf{xx}\, \mathrm{d}^2 A, \qquad (2.4)$$

$$V_1^{r,s} = \frac{1}{4}\int_{\partial P} \mathbf{x}^r \mathbf{n}^s\, \mathrm{d}^1 S, \qquad (2.5)$$

$$V_2^{r,s} = \frac{1}{2\pi}\int_{\partial P} c\, \mathbf{x}^r \mathbf{n}^s\, \mathrm{d}^1 S. \qquad (2.6)$$

In practice, however, we need not consider all of these tensors, because some of them are linearly dependent [23]. It can be shown that only the following tensors carry independent information:

$$V_0^{2,0} = \int_K \mathbf{xx}\, \mathrm{d}^2 A, \qquad (2.7)$$

$$V_1^{2,0} = \frac{1}{4}\int_{\partial K} \mathbf{xx}\, \mathrm{d}^1 S, \quad V_1^{0,2} = \frac{1}{4}\int_{\partial K} \mathbf{nn}\, \mathrm{d}^1 S, \qquad (2.8)$$

$$V_2^{2,0} = \frac{1}{4}\int_{\partial K} c\, \mathbf{xx}\, \mathrm{d}^1 S. \qquad (2.9)$$

In the following we will only consider these second-rank tensors. They are listed together with their names in Table 1. The numerics for calculating the Minkowski valuations for pixelized data sets is described in [33], the

---

[1] First-order moments with the normal vectors always vanish, as is shown in [32]

Table 1. The Minkowski valuations used in this paper.

Symbol	Formula	Name
V_0	$\int_P \mathrm{d}^2A$	area
$\mathbf{p}_0$	$\int_P \mathbf{x}\mathrm{d}^2A/V_0$	center of mass
$V_0^{2,0}$	$\int_P \mathbf{xx}\mathrm{d}^2A$	mass tensor
V_1	$\int_{\partial P} \mathrm{d}^1S$	length of perimeter
$\mathbf{p}_1$	$\int_{\partial P} \mathbf{x}\mathrm{d}^1S/V_1$	center of perimeter
$V_1^{2,0}$	$\int_{\partial P} \mathbf{xx}\mathrm{d}^1S$	perimeter tensor
$V_1^{0,2}$	$\int_{\partial P} \mathbf{nn}\mathrm{d}^1S$	$\mathbf{n}$-weighted perimeter tensor
V_2	$\int_{\partial P} c\mathrm{d}^1S$	Euler characteristic
$\mathbf{p}_2$	$\int_{\partial P} c\mathbf{x}\mathrm{d}^1S/V_2$	curvature centroid
$V_2^{2,0}$	$\int_{\partial P} c\mathbf{xx}\mathrm{d}^1S$	curvature tensor

theoretical foundations for the numerics are given in [34], Ch. I.3 and Appendix A.2.

Because of motion covariance, the numerical values of the second-rank Minkowski tensors depend on the choice of the coordinate system. But in many applications, there is a natural choice for the origin of the coordinate system. For our neuronal cells we will take the center of the soma as the origin (in other cases it might be useful to calculate the second-rank Minkowski tensors $V_i^{r,s}$ with respect to the corresponding centroids $\mathbf{p}_i$ for $i = 0, 1, 2$).

In order to illustrate how the Minkowski valuations work for pixelized data sets, let us consider three simple toy examples (some more examples can be found in [33]). They are shown in Figure 1. The red filled square, the blue open square and the yellow cross denote the centroids $\mathbf{p}_0$, $\mathbf{p}_1$ and $\mathbf{p}_2$, respectively. The tensors are calculated around the center of the black square in the middle of the pixel sets as origin. The red, blue and yellow ellipses within the neurons visualize the tensors $V_0^{2,0}$, $V_1^{2,0}$ and $V_2^{2,0}$, respectively. The ellipse for the tensor $V_1^{0,2}$ is shown at the left-hand side. The equation defining the ellipses is always: $\mathbf{x} = \mathbf{c} + a(\frac{\tau_>}{\tau_<}\cos(\phi)\mathbf{e}_> + \sin(\phi)\mathbf{e}_<)$, where ϕ runs from 0 to 2π, $\mathbf{e}_>$ ($\mathbf{e}_<$) is the eigenvector corresponding to the larger (smaller) eigenvalue $\tau_>$ ($\tau_<$) of the tensor and $\mathbf{c}$ is the center of the soma (except for $V_1^{0,2}$; its ellipse is shifted to the edge of the panels). So the axis ratios of the ellipses are the ratios of the eigenvalues, and the ellipses point into the direction of the eigenvector with the larger eigenvalue. The size of the ellipses does not carry specific information, since the scale factor $a > 0$ is freely chosen for each tensor (roughly, we use the a's for equalizing the minor axes of the ellipses).

In the top panel of Figure 1 the pixel set displays an axial symmetry and is almost point symmetric. Accordingly, the centroids are very close to each other; they fan out along the symmetry axis. The tensors $V_i^{2,0}$ align perpendicular to the symmetry axis, because the whole pixel set is more elongated along the horizontal axis. The tensor ellipses for the mass tensor $V_0^{2,0}$ and the perimeter tensor $V_1^{2,0}$ almost coincide, whereas the ellipse corresponding to $V_2^{2,0}$ is a bit more elongated. The reason is that the corners, which play an important role for the curvature tensor $V_2^{2,0}$ are further away from the middle black square, which only contributes to $V_0^{2,0}$ and $V_1^{2,0}$.

For the middle panel, the pixel set has been slightly modified: in order to destroy the symmetry, we rearranged one of the "arms". As a consequence, the average pixel is lower down than in the first panel, and all centroids move downwards. The effect is most prominent for the curvature centroid $\mathbf{p}_2$, because it depends on corners, some of which disappear for the rearranged "arm". Note, furthermore, that the centroids span a non-degenerate triangle, a fact that indicates asymmetry. The lack of symmetry is also reflected by the tensor ellipses, which are not parallel any more. Note, furthermore, that the ratios between the bigger and the smaller eigenvalues are larger for the second pixel set. The reason is that — due to the "movement" of the upper right arm — the vertical extension of the pixel set shrinks on average, such that the pixel set is more elongated.

The bottom panel shows a variation of the pixel set in the middle panel, where two holes have been added. Accordingly, the Euler characteristic becomes −1. There is no big effect on both $\mathbf{p}_0$ and $\mathbf{p}_1$ and the related tensors. $\mathbf{p}_2$, however, undergoes a big jump, and the ellipse for the curvature tensor $V_2^{2,0}$ is twisted and more elongated. The position of $\mathbf{p}_2$ can be explained as follows: the hole at the right-hand side makes a big negative contribution to $\mathbf{V}_2$. So, if $\mathbf{V}_2$ is calculated around the center of the black square, it points to the left hand side. But since the Euler characteristic V_2 itself is negative, $\mathbf{p}_2$ is bounced back to the right hand side due to its normalization through V_2. For the major axis of the curvature tensor ellipse, there is some kind of repulsion from the right hole, because this hole makes a big negative contribution to the tensor; the effect of the other hole is much smaller because it is closer to the soma.

The tensor $V_1^{0,2}$ is shown at the left hand side. It always aligns parallel to the grid axes. The reason is that it crucially depends on normals that can only point into four directions for a square lattice[2]. The shape of the $V_1^{0,2}$ ellipse can be understood as follows: the eigenvalues of $V_1^{0,2}$ count the number of bonds with horizontal or vertical normals, respectively. For our toy examples, there are more vertical normals, so the tensor is anisotropic. By moving from the top to the middle panel, more horizontal than vertical normals are destroyed; in this way the tensor becomes even more anisotropic.

Let us conclude this section by adding two comments. First, note, that by considering the eigenvalues of a tensor with respect to an origin which is given by the body itself, motion-invariance is regained. But does this mean that we have been returning to the scalar Minkowski functionals themselves? The answer is no. Additivity has been lost, because forming eigenvalues is not a linear operation, and, as a consequence, the eigenvalues of a Minkowski tensor cannot be decomposed in the same way as the area is. So

---

[2] For an elementary proof of this, you can start with a single pixel and then proceed by using additivity.

we have significantly extended the Minkowski framework without having given up its conceptual foundations.

Second, there is a natural extension of our framework to three-dimensional neuron data. In three dimensions, there are four scalar Minkowski functionals, viz. the volume, the area, the integrated mean curvature and the Euler characteristic (see [35] for definitions). Higher-rank Minkowski tensors are moments of these quantities. There are four centroids and a number of related tensors. They can be calculated for smooth bodies as well as for voxel sets (see [33]).

3 The analysis of pixelized neuron data

Data. We analyze two-dimensional data of 10 prototypical neuronal cells, made available by the courtesy of Prof. Berson [27]. This subset of cell images were obtained from 43 cats of various ages following the appropriate animal care guidelines. Staining was revealed using Lucifer Yellow immunohistochemistry [36], and observed by means of epifluorescence illumination. Camera lucida drawings were obtained for selected cells. Ganglion cells were morphologically classified taking into account soma size, dendritic field size and structure, retinal location and dendritic stratification, see [37]. Cells were recognized as being members of various established types, (α, β, δ, ϵ, η, ι, κ, λ, θ, ζ). See [36] and references therein for a detailed description of the experimental procedure and cell classification. We have one cell per cell type. Each cell is represented as a subset of filled pixels within a square lattice. The physical scale of one pixel is about 1.8 μm. Not all of the neuron pixel sets are connected; some of them consist of disconnected parts.

Method. We start from a pixel set P representing a cell. We first apply a *binary dilation* as known from mathematical morphology, see [20], Ch. 3. The structuring element is chosen to be a sphere of radius r_s. As a result we get a new pixel set P_{r_s} comprising all pixels for which the distance from some pixel of P is no more than r_s, see [38]. In more intuitive terms, this set can be interpreted as the "influence area", i.e. that part of space for which interactions with the neuron are possible, given that the interactions are confined to distances no larger than r_s (ib.). Two dilations of our λ neuron with $r_s = 2$ pixels and $r_s = 8$ pixels, respectively, are presented in Figure 2. They show that *dilations bring out structure at different scales.* Consider, for instance, the area V_1. Whereas, for small r_s, the area is dominated by details of the dendrites, for larger r_s, V_1 reflects the overall structure of the cell.

We call r_s *dilation scale.* It will always be measured in units of pixels. In order to be sensitive to structures at different scales, we will not stick to a particular r_s, but rather consider a series of dilations with increasing dilation scale r_s. We will calculate our characteristics for each dilation scale and show them as a function of dilation scale. For instance, we will calculate $V_0(P_{r_s})$ for various r_s and regard this as a function $V_0(r_s)$. Such a function can then be compared for different cells. We thus get a *multiscale analysis.*

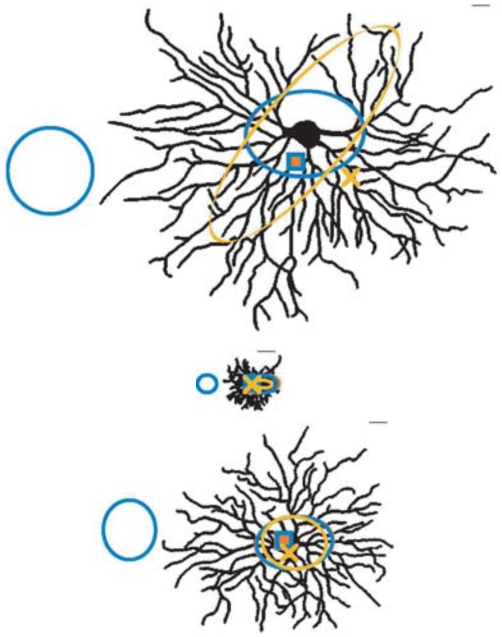

Fig. 3. The neurons of type α (top panel), β (middle panel) and δ (bottom panel). The pixel sets are dilated, the dilation scale is one pixel. The meaning of the points and the ellipses is explained in Figure 1. The small dash in the upper right corner of each panel has a length of 20 pixels (i.e. 36 μm). The pictures are based on data obtained by [27] (their figure No. 5, copyright permission by Nature Neuroscience). Note, that in all panels of this figure as well as of Figures 4 and 5 the tensor ellipses for $V_0^{2,0}$ and $V_1^{2,0}$ almost coincide.

For calculating the Minkowski tensors at some particular r_s, we choose the center of the soma as a "natural" origin. The soma and its center are identified visually, in an interactive way.

4 Results and discussion

Qualitative results. We show the neurons with some of the results for a dilation scale of one pixel in Figures 3–5[3].

Let us start with some qualitative observations. First, the centroids $\mathbf{p}_0$ through $\mathbf{p}_2$ are typically not within the soma. Recalling that the centroids are morphological centers, we can equivalently say that the soma is quite often eccentric. It would be interesting to know whether the eccentricity of the soma is characteristic for some types of neurons. We suspect that the eccentricities depend on the function and the local environment of the cells. Further investigations are needed to explore this effect.

---

[3] In the following, one has to be cautious in interpreting the yellow ellipses, because, for our neuronal cells, the tensor $V_2^{2,0}$ sometimes has one or two negative eigenvalues. In this case, the ellipse will become smaller than the other ellipses and point into the direction of $\mathbf{e}_<$ instead of $\mathbf{e}_>$, if $|\tau_>| < |\tau_<|$.

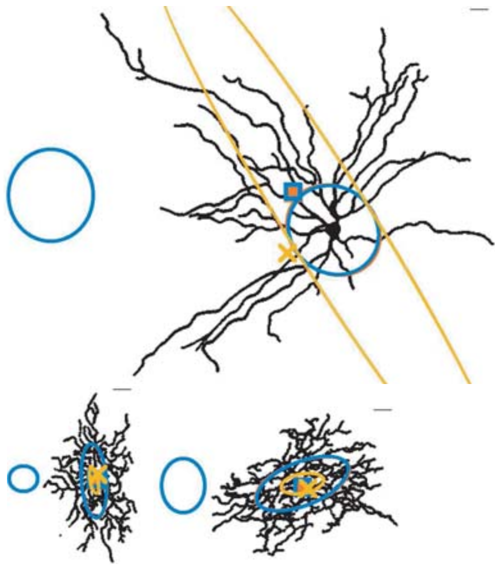

Fig. 4. Neurons of type ϵ (top panel), η (bottom left panel) and ι (bottom right panel). The dilation length is one pixel. The pictures are based on data obtained by [27] (their figure No. 5, copyright permission by Nature Neuroscience).

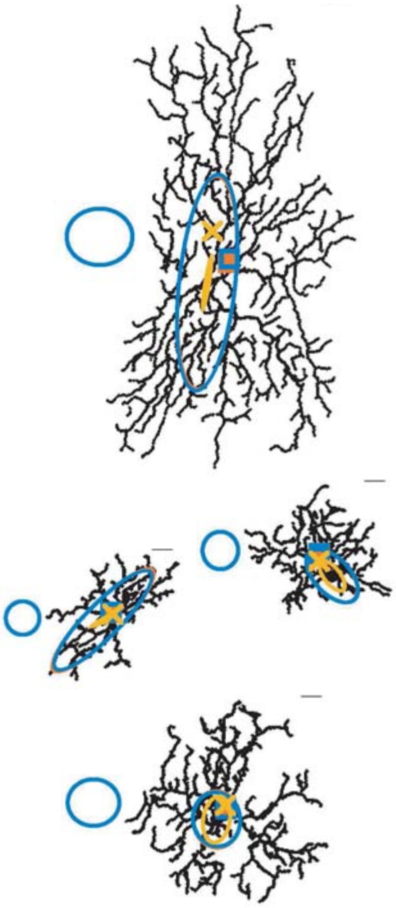

Fig. 5. Neurons of type κ (top panel), ζ (middle left panel), θ (middle right panel) and λ (bottom panel). The dilation scale is one pixel. The pictures are based on data obtained by [27] (their figure No. 5, copyright permission by Nature Neuroscience).

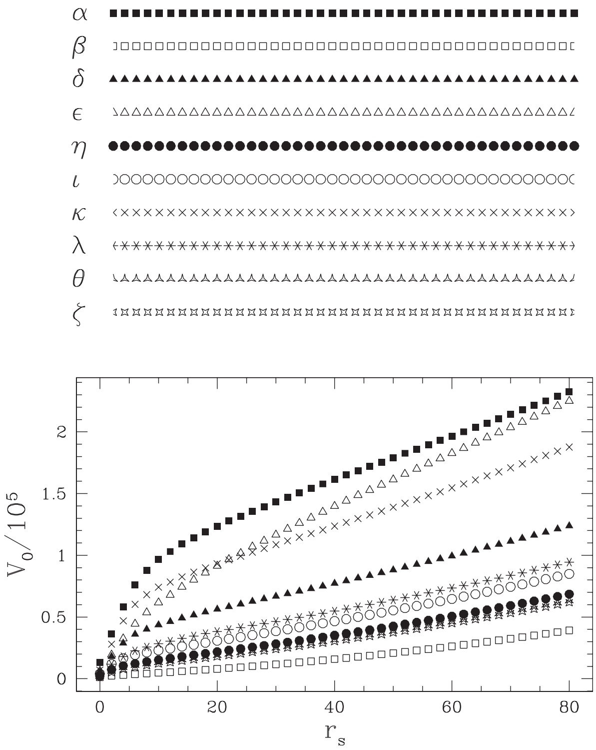

Fig. 6. Top panel: the point styles denoting the different cell types. Bottom panel: the volume V_0 as a function of r_s for a large range of r_s-values.

Second, we observe that typically $\mathbf{p}_0$ and $\mathbf{p}_1$ almost coincide, whereas $\mathbf{p}_2$ may be further away from them. Something similar is true about the tensors: the tensor ellipses of $V_0^{2,0}$ and $V_1^{2,0}$ often closely resemble each other, whereas the ellipse for $V_2^{2,0}$ greatly differs. The reason is as follows: As our toy examples have shown, $\mathbf{p}_2$, $V_2^{2,0}$ and the corresponding Minkowski functional (viz. the Euler characteristic) are sensitive to holes. For positive Euler characteristics, every hole that is off-soma pushes $\mathbf{p}_2$ onto the other side of the soma. As a consequence, the location of $\mathbf{p}_2$ and the form of $V_2^{2,0}$ very much depend on the holes, their shapes and their positions. The holes in turn depend on tiny details of the branching structure that are neither reflected in $\mathbf{p}_0$ and $\mathbf{p}_1$ nor in the tensors $V_0^{2,0}$ and $V_1^{2,0}$. — Note, that most of the holes are probably due to the projection of the neuron into two dimensions.

We will now turn to a more quantitative analysis. We show the first scalar Minkowski functional, V_0, for a broad range of dilation scales r_s in the bottom panel of Figure 6, where the point styles designating the different cell prototypes are explained in the top panel. For $r_s < 5$, V_0 typically grows very quickly, as r_s increases. For larger dilation scales, $r_s > 10$, typically a more moderate growth can be seen. For some neurons, $V_0(r_s)$ appears to be linear in this range of dilations scales; for other neurons, $V_0(r_s)$ is a convex function in this range of r_s. Bigger neurons typically grow faster than smaller ones for these r_s-values. The explanation is as follows: as r_s increases, the arms of the cells' arborizations are blown up, and the volume V_0

is growing accordingly. However, when different arms begin to overlap each other, no additional pixels are filled, if r_s is further enhanced. Therefore, as soon as overlaps become significant, the growth of V_0 slows down. At some value of r_s, the whole pattern of arms will be covered by pixels, and only the outer parts of the cell will contribute to the growth of V_0.

For a better understanding, let us look closer at the β cell. Its overall shape is roughly spherical, and its extension $2r_0$ is about 60 pixels. If the β cell is dilated with a sufficiently large r_s ($r_s > 10$), the dendritic fine structure is completely covered, and the dilated cell is not that far from a circle of radius r_0 dilated by r_s. Thus, for sufficiently large r_s-values, the volume of the dilated cell is about

$$V_0 \approx \pi(r_0 + r_s)^2 = \pi r_0^2 + 2\pi r_0 r_s + \pi r_s^2, \qquad (4.10)$$

which is parabolic in r_s. If this approximation is reasonable for a broad range of r_s-values for which $r_s < r_0$, the quadratic term πr_s^2 can be neglected, and the function $V_0(r_s)$ appears to be linear in this range.

More generally, let CP denote the convex hull of a pixelized data set P (or, more precisely, a pixel approximation of its convex hull). For sufficiently large dilation scales r_s, dilations of P and CP, call them P_{r_s} and CP_{r_s}, respectively, are close to each other; consequently, the difference $V_0(P_{r_s}) - V_1(CP_{r_s})$ is small compared to $V_0(P_{r_s})$. The size of CP_{r_s} can be calculated using *Steiner's formula* (see [30], p. 367, e.g.):

$$V_0(CP_{r_s}) = V_0(CP) + r_s 4V_1(CP) + \pi r_s^2. \qquad (4.11)$$

This is again a parabola, where the Minkowski functionals V_0 and V_1 of CP enter as coefficients. As a consequence, if r_s is large enough, the volume $V_0(P_{r_s})$ can be approximated by the r.h.s. of equation (4.11). It is thus approximately a quadratic function of r_s and might appear to be linear for a certain range of r_s-values. The shape of the parabola is determined by the scalar Minkowski functionals of the convex hull CP. Bigger neurons will have larger values of $V_0(CP)$ and $V_1(CP)$ such that their $V_0(r_s)$ is larger and has a larger slope[4].

In order to observe the fine-grained structure of the cells where the neurons significantly differ from their convex hull, we have to concentrate on smaller dilation scales $r_s < 20$.

The top panel in Figure 7 shows more closely that, for many neurons, there is a transition or crossover between a quick and a moderate growth in V_0 around $r_s \approx 5$. For some bigger neurons (α, δ, κ, e.g.), this crossover can be observed as a bend around $r_s = 5$.

The medium panel in Figure 7 shows that, for small r_s, V_1 decreases as a function of r_s. The reason is that, in this range of r_s, V_1 is dominated by small scale features that are "swallowed" stepwise. V_1 reaches a constant value later on. The reason is as follows. As r_s increases, V_1 will gain at the outer parts of the cells, but lose in the inner parts, because holes are being filled. Gains and losses roughly compensate each other. Note, that the curves for the α, δ and κ cell type show an inflection point, which roughly coincides with the location of their bends in V_0.

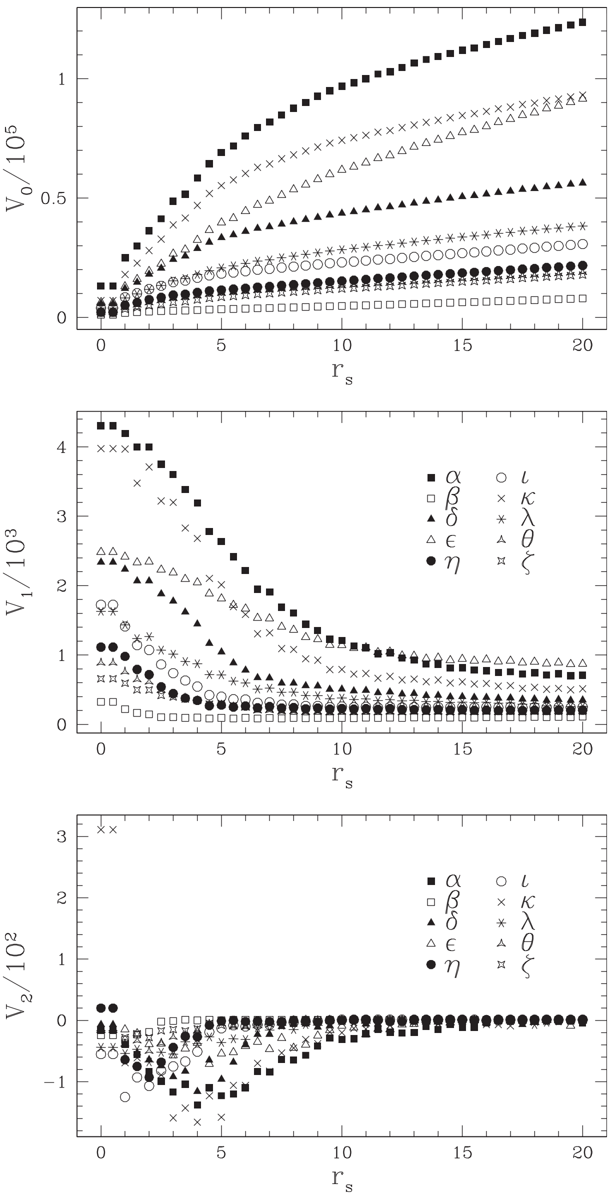

Fig. 7. The scalar Minkowski functionals as functions of the dilation scale for all cells. (Note, that in the first panel the curve for the θ cell is between the curves for the η and ζ cells.)

The curves for the Euler characteristic (bottom panel in Fig. 7) display a number of jumps. One reason is that the Euler characteristic takes only whole numbers as values. Another reason is that the Euler characteristic is sensitive to holes, which in turn depend on tiny details that change continually, as the cells are dilated. But there is also some more general pattern. The negative values to be

---

[4] Similar considerations apply to V_1. Note also, that equations (4.10) and (4.11) are strictly speaking only valid for convex bodies (which CP — some pixel approximation of a convex hull — isn't necessarily). For pixel sets as investigated in this paper, additional factors arise in the r_s expansions, and the equations hold only up to some corrections. But this does not invalidate our argument.

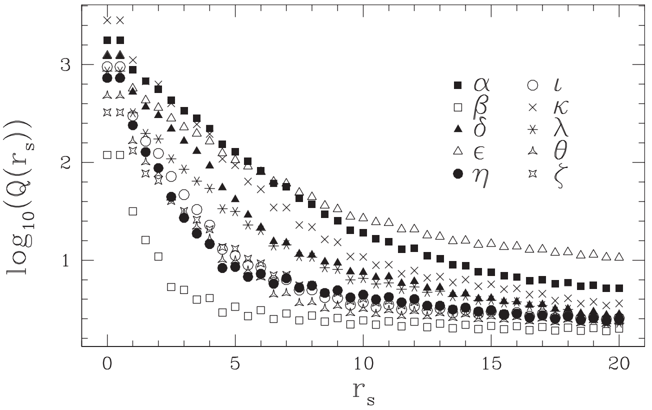

Fig. 8. The logarithm of Q (a variety of the isoperimetric ratio) as a function of r_s.

found most often indicate that the cells are dominated by holes. For the bigger cell types (α, δ, ϵ and κ), there is a characteristic dip for small r_s. Up to this point, additional holes are formed, as branches of the neuron start to touch each other. The minimum of the dip roughly seems to coincide with the point where V_0 shows the crossover between the two different kinds of growth.

A useful way of combining the information present in the scalar Minkowski functionals is to construct the following dimensionless quantity Q:

$$Q := \frac{4V_1^2}{\pi V_0}\,. \tag{4.12}$$

This is a variation of the so-called isoperimetric ratio. For a convex body P, we have $Q(P) \geq 1$, where the equality holds for a circle [39–41][5]. Q is considerably larger than one, whenever the body under investigation has an "excess perimeter" as compared to its area. We show the logarithm of Q as a function of r_s in Figure 8. The interpretation is as follows: for small dilation scales r_s, most of the dendrites are still present producing excess areas, so Q starts with very high values. As the dilation scale increases, Q goes down. The α, ϵ and κ cells have the largest Q-values, whereas the β-cell has the lowest Q-values for a large range of dilation scales, because of its overall spherical shape. For $r_s < 6$, the decrease in $\log_{10}(Q)$ seems roughly to be linear; the slopes vary with the cell type.

In Figures 9 and 10 we consider the centroid distances $\mathbf{p}_i$-soma, dis$_i$. For $i = 0$, they are relatively stable as a function of r_s, whereas, for $i = 1$, more variation can be observed. How is this to be explained? Consider the κ neuron (Fig. 5) and the crosses in Figure 9 as an example. The soma of the κ cell is located in the lower half of the neuron (in Fig. 5 it is covered by parts of the ellipse for $V_2^{2,0}$). Moreover, in the lower half of the κ cell the distribution of small arms is a bit denser than in the upper half. Consequently, for small r_s, there is a significant contribution to the perimeter from this part, and accordingly the center of perimeter $\mathbf{p}_1$ stays in the lower half. For larger $r_s \approx 10$, however, the lower, denser part is filled more quickly, whereas in the upper part quite big holes are left, which significantly contribute to the perimeter. As a consequence, the position of $\mathbf{p}_1$ moves upwards and away from the soma, such that dis$_1$ becomes larger. Later, when these big holes are filled as well, $\mathbf{p}_1$ approaches the soma again, such that dis$_1$ becomes smaller. In this way the curve for dis$_1$ contains very detailed information about the morphology of the neuron.

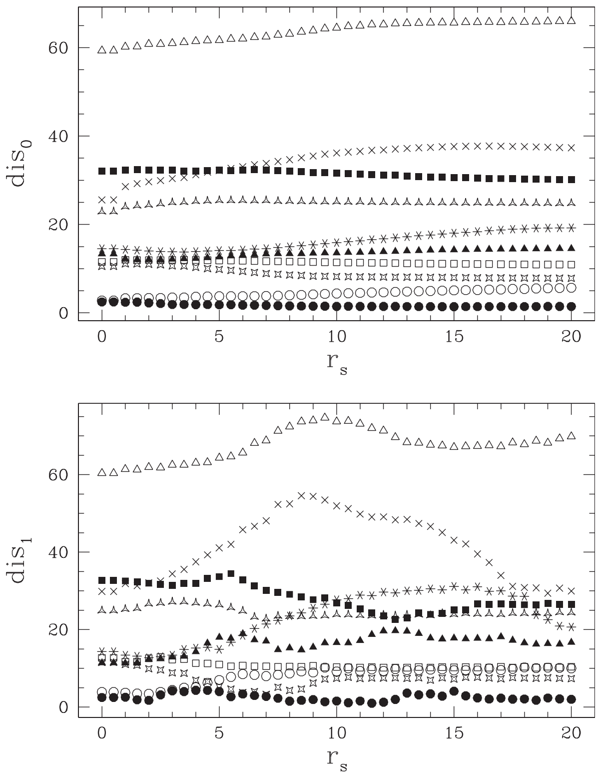

Fig. 9. The distances soma — $\mathbf{p}_0$ (top panel) and soma — $\mathbf{p}_1$ (bottom panel) as functions of the dilation scale.

In terms of dis$_0$ and dis$_1$ the soma is most eccentric for the ϵ neuron. This is also reflected in our visual impressions. It might be useful, however, to normalize the dis$_i$ parameters by some estimate of the cell size. If we would do so, smaller cells would have a reasonable chance of having bigger eccentricities.

For $i = 2$, (Fig. 10) we observe even larger variations of the centroid distances. Plateaus alternate with jumps that can ultimately be traced back to jumps in the Euler characteristic. For small neurons, such as the β type, however, there is not much variation, because the cell is very small and gets completely filled soon. For the α, δ and ϵ-type, there is a common pattern: As the dilation scale increases, the jumps become larger. The reason is probably that, for larger dilation scales, only a few holes will appear far off the center. When one of these outer holes disappears, $\mathbf{p}_2$ jumps considerably.

In Figures 11 through 13 we consider the anisotropy of the cells. In order to quantify anisotropy we take the eigenvalues of the tensors $V_i^{j,k}$, $\tau_>$ and $\tau_<$ and calculate the quantity anis $:= 2(\tau_> - \tau_<)/(|\tau_>| + |\tau_<|) \leq 2$. The

---

[5] For a pixel approximation of a circle, Q is larger than 1, but this does not matter for our purposes.

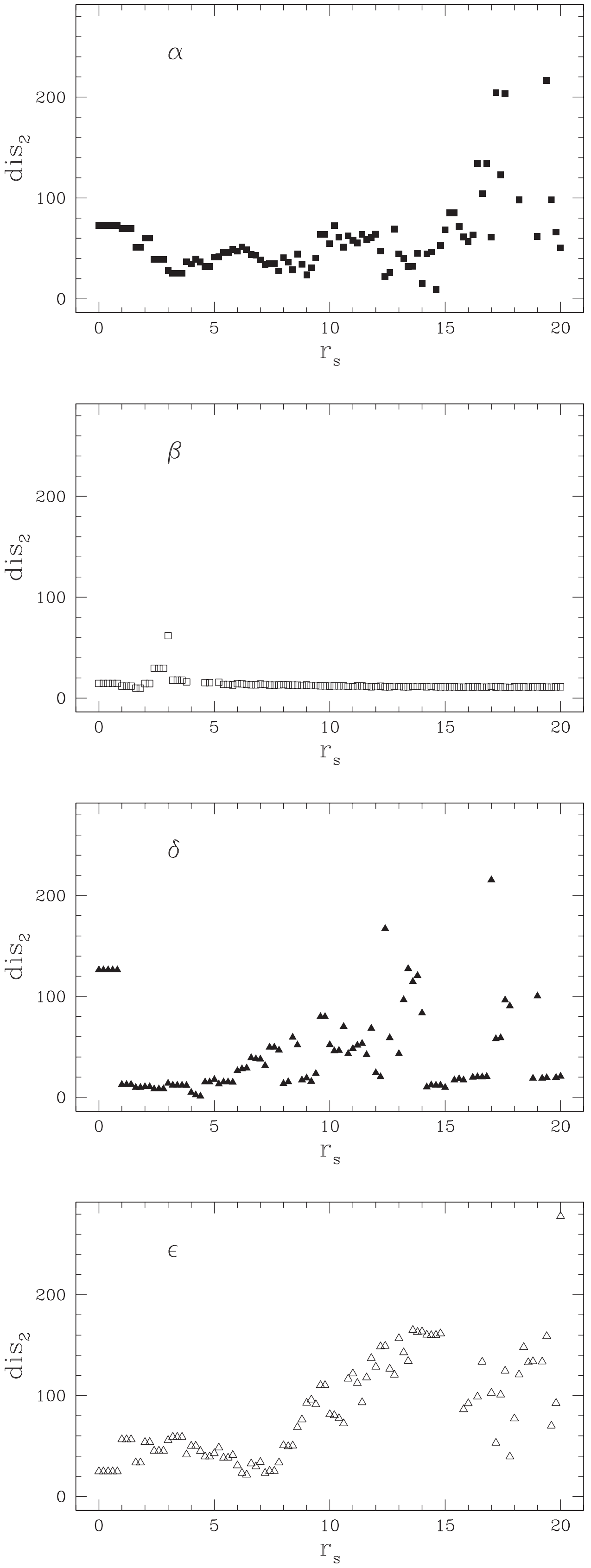

Fig. 10. The distances soma — $\mathbf{p}_2$ as a function of the dilation scale for four cells. If $\mathbf{p}_2$ is not defined for some r_s (because of $V_2 = 0$), no point is shown.

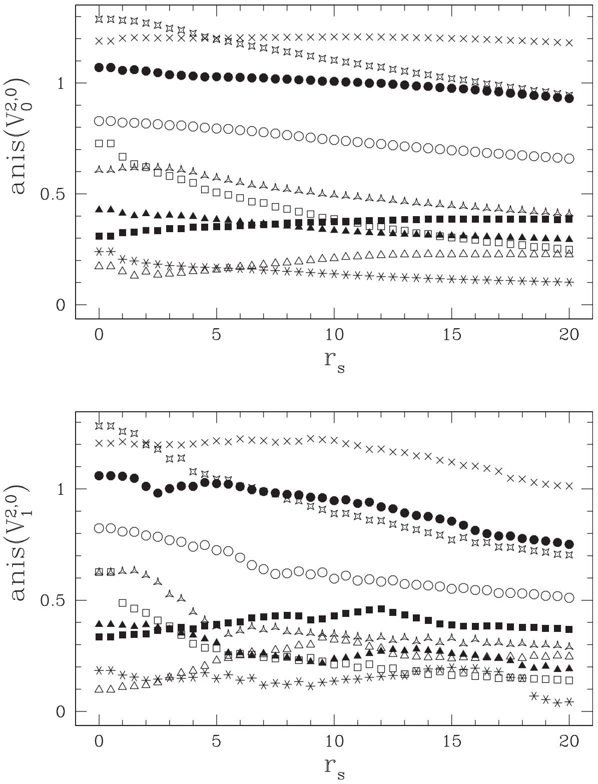

Fig. 11. The anisotropy parameters derived from the mass tensor $V_0^{2,0}$ (top panel) and the perimeter tensor $V_1^{2,0}$ (bottom panel) as functions of the dilation scale.

anisotropy parameters derived from different tensors focus on different kinds of anisotropy (the area elements belonging to a body might be distributed differently from those of its perimeter elements, for instance). As can be seen from Figure 11, the anisotropies in $V_0^{2,0}$ and $V_1^{2,0}$ are quite stable; most often they decrease slowly, as the dilation scale increases. This indicates that the cells display large-scale anisotropies that are not destroyed by dilating the cell. For some cells (η, κ, ζ), the anisotropies are considerable. For each cell type, the anisotropies of area and perimeter do not differ greatly. The $V_1^{2,0}$ tensor is a bit more sensitive to small-scale variations of the morphology, however; so the anis($V_1^{2,0}$)-r_s curves appear less smooth than the anis($V_0^{2,0}$)-r_s curves. On the other hand, across the range of cell types, the variation is quite high. Thus anisotropies seem to have a significant discriminative power.

It is different with the tensor $V_2^{2,0}$, which is considered in Figure 12. The anisotropy derived from this tensor jumps back and forth and sometimes reaches values that exceed those derived from the other tensors. This performance should not come as a surprise, since we have already seen that other characteristics that are related to the Euler characteristic such as $\mathbf{p}_2$ typically show jumps. At some point, however, when the dilation has produced one connected pattern and no new holes will be formed any more by increasing r_s further, the anisotropy becomes smoother. This point is reached very early for the β cell

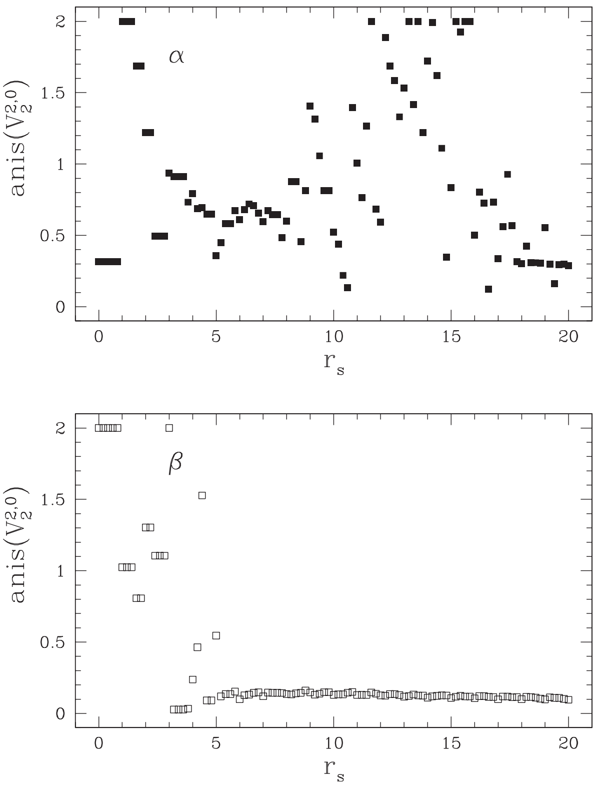

Fig. 12. Another anisotropy parameter (derived from $V_2^{2,0}$) for two cells as a function of the dilation scale.

and therefore visible in the bottom panel of 12. Apart from this, the dependence on r_s looks rather erratic and irregular.

As mentioned before, on the square lattice, the last tensor to be considered, $V_1^{0,2}$, has a simple interpretation. It checks whether the majority of normals are parallel to the horizontal or to the vertical grid axis. If ∂P is dominated by vertical or horizontal normals, $V_1^{0,2}$ will display a corresponding anisotropy; if not, $V_1^{0,2}$ will roughly be isotropic. Figure 13 shows results for selected neurons. If we compare to the anisotropies considered above, the anisotropy arising from $V_1^{0,2}$ is quite small. For small values of the dilation scale, anis($V_1^{0,2}$) is not so much influenced by the overall shape of the neuron, but rather by the directions of the single arms. Interestingly, the graphs shown are qualitatively different for the different types of cells: One cell (viz. the α cell) starts with zero anisotropy, whereas others begin with a non-zero anisotropy. Moreover, sometimes significant peak structures can be observed. But because of its relation to normals, $\mathbf{n}$, the value of $V_1^{0,2}$ depends to a large extent on the orientation of the cell with respect to the grid. For this reason $V_1^{0,2}$ is only of limited use.

In Figure 14, the *traces* of the tensors $V_i^{2,0}$ are considered (the trace of the fourth tensor, $V_1^{0,2}$ need not to be taken into account at this point, because it equals V_1). Qualitatively, the viewgraphs for $V_i^{2,0}$ resemble the curves of their scalar counterparts, V_i for $i = 0, .., 2$. In order to

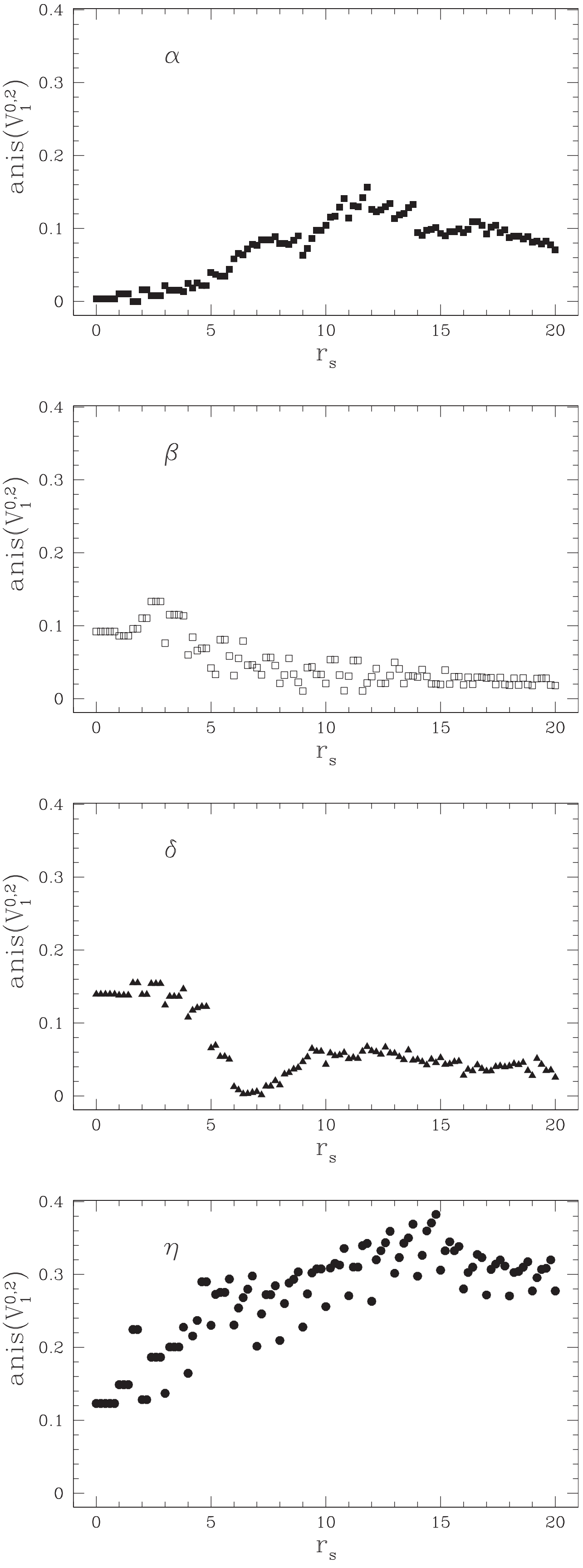

Fig. 13. The anisotropy parameter derived from $V_1^{0,2}$ for four cells as a function of the dilation scale.

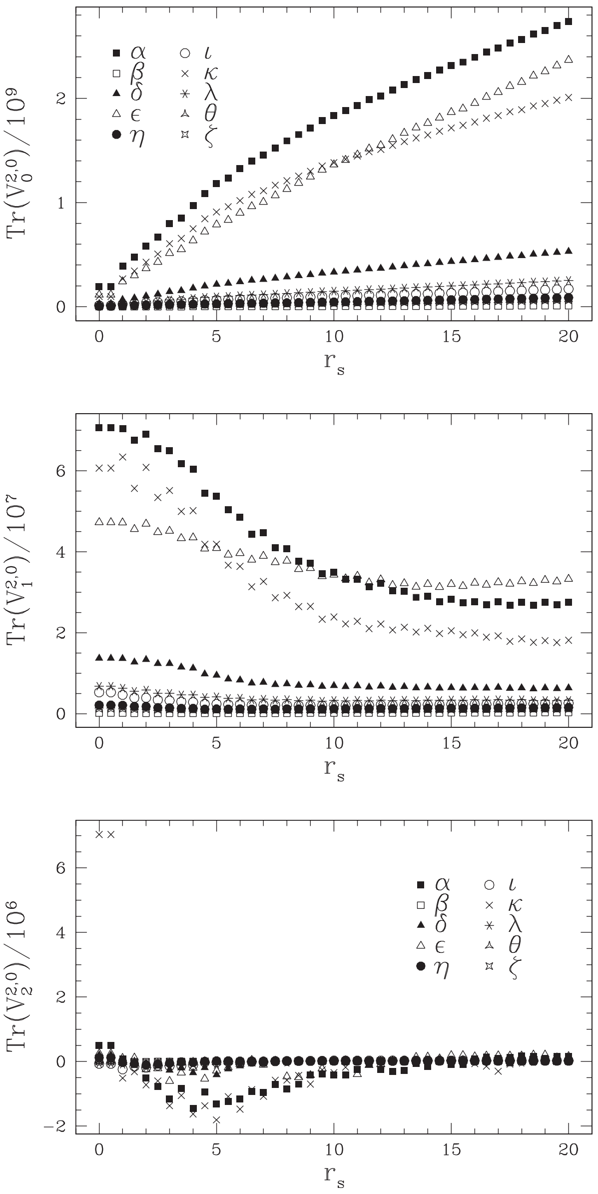

Fig. 14. The traces of the tensors $V_i^{2,0}$ for $i = 0, .., 2$ as functions of the dilation scale.

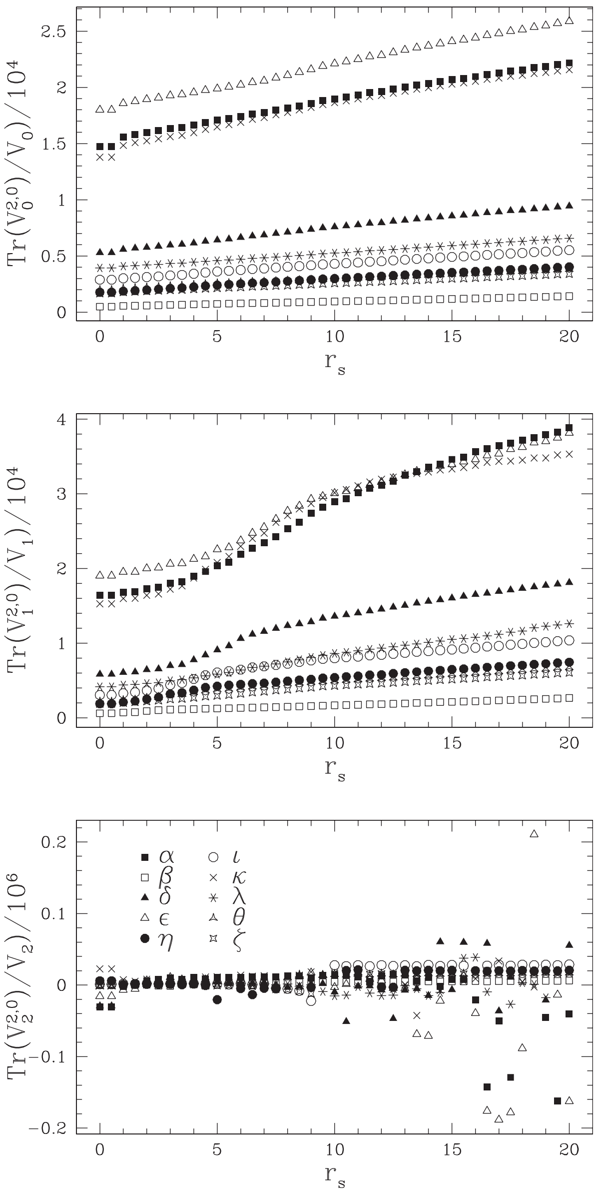

Fig. 15. The traces of $V_0^{2,0}$, $V_1^{2,0}$, and $V_2^{2,0}$, now normalized by the corresponding scalars V_0, V_1 and V_2, respectively. If $V_2 = 0$ for some r_s, no data point is shown at all.

extract more specific information, it is thus useful to divide $\mathbf{Tr}(V_i^{2,0})$ by V_i, respectively, for $i = 0, .., 2$. The result is a measure of how concentrated a cell is in terms of area, perimeter or curvature: $\mathbf{Tr}(V_0^{2,0})/V_0$, for instance, will be the bigger, the further the soma and those parts of the cell that bear most of its volume lie apart.

Results can be seen from Figure 15. $\mathbf{Tr}((V_0^{2,0})/V_0$ increases continuously, as r_s is enhanced. The reason is that more pixels are added at the outer parts of the neuron, so the neurons become less concentrated.

In $\mathbf{Tr}((V_1^{2,0})/V_1$ there is a kink at least for some neurons (α, δ, ϵ, κ). It indicates an additional growth effect. It is probably due to the fact that, for small r_s, the little branches within the cell significantly contribute to $V_1^{2,0}$, thus the neuron appears to be very concentrated; for larger values of r_s, the arms merge and do not contribute to the perimeter any more, so most of the neuron's perimeter is found at its outer parts and $\mathbf{Tr}((V_1^{2,0})/V_1$ is comparatively large. In between, the growth of $\mathbf{Tr}((V_1^{2,0})/V_1$ is disproportionally high. Note, that for the α, δ and κ cells, the kinks roughly set in at the r_s-locations of the bend in V_0, which roughly coincide with the positions of the inflection points in V_1.

Constructing global measures. The multiscale analysis presented in this paper leads to rich and detailed information on the geometric aspects of an object. Nevertheless, once such a description of the data has been obtained, it is often useful to derive a compact set of global measures that summarize the most important morphological aspects. In this paper, we consider several ways of condensing multiscale information into simple parameters: The *monotonicity index* [18,19] is defined as

$$i_s = \frac{s}{s+d+p}, \tag{4.13}$$

where s, d and p count each time the function increases, decreases and remains unchanged, respectively. Thus i_s quantifies the fraction of the interval where the function is monotonically increasing. The *mean value* is the average value of the function over the interval. The *half scale* is the scale at which the area below a curve reaches half of its total value. A different way of constructing global parameters is to consider the *slope* of some characteristic in some particular range of r_s-values[6].

In Figure 16 we visualize the average slopes of V_0 in the range $r_s \in [10, 60]$ and of $\log_{10}(Q)$ in the range $r_s \in [1.5, 4.5]$ for the different cells. In both cases we choose a range of r_s-values for which the functionals under investigation look roughly linear for most cell types. From Figure 16 it is clear that the slopes do indeed discriminate amongst the cell prototypes.

In order to further illustrate our approach, we selected two feature spaces, which are spanned by global, size-independent morphological characteristics. In order to calculate these global measures, we considered the interval $r_s \in [0, 20]$ and a spacing of 0.2.

Our first feature space is spanned by the mean of the anisotropy parameter derived from $V_0^{2,0}$, $\overline{\text{anis}}(V_0^{2,0})$, and the mean of the anisotropy parameter corresponding to $V_0^{2,0}$, $\overline{\text{anis}}(V_1^{2,0})$. It is shown in Figure 17a. There appears to be some systematic correlation between both characteristics: cells with higher $\overline{\text{anis}}(V_0^{2,0})$ tend to have higher $\overline{\text{anis}}(V_1^{2,0})$ as well. Given our qualitative observations above, this should not come as a surprise, although it is in principle possible to have high anisotropy in $V_0^{2,0}$ and low anisotropy in $V_1^{2,0}$. Thus, for discriminating between different cells, one dimension of this feature space is essentially redundant. But the presence of some correlation may indicate some common trait shared by all cell prototypes.

A different situation can be observed for our next feature space. It is spanned by the monotonicity index $i_s(\text{dis}_0)$ and by the half scale $h(\mathbf{Tr}(V_1^{2,0}))$. As can be seen from Figure 17b, the scatterplot displays more scatter, and clusters can be recognized in the feature space.

Although the methodology proposed in this paper may have a bearing on the classification of cat ganglion cells, it is difficult to draw more definitive conclusions at this point, because the original classification [28] takes into account not only the neuronal morphology, but also the cell stratification and the size of the soma. Moreover, except for the more common α and β types, only a small number of examples of the cell types have been analyzed in the literature [28]. A more detailed examination of which feature spaces are most useful has to wait for further data.

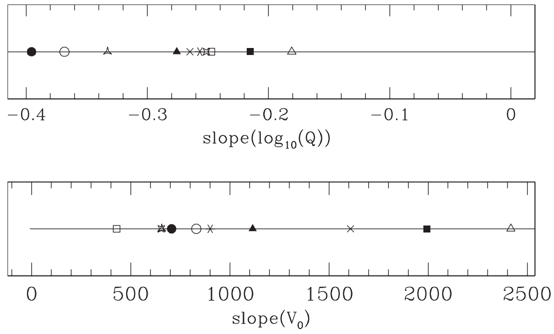

Fig. 16. The slopes of V_0 (bottom panel) and $\log_{10}(Q)$ (top panel) for the different cells. The point styles are the same as in the top panel of Figure 6.

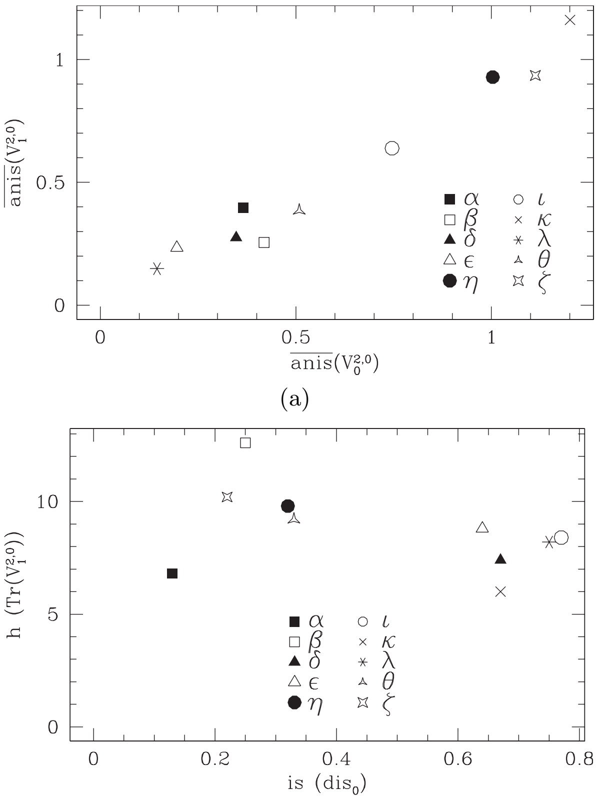

(a)

(b)

Fig. 17. Scatter plots from selected features of an extended Minkowski analysis showing the population of the feature space with the neuronal cells.

Relation to other morphological measures. In order to put Minkowski valuations into the perspective of previous works, we note that [2] group morphological measures into four classes, namely "overall cell morphology", "territorial coverage", "cell density, overlap and connectivity" and "hierarchical structure of arborizations".

---

[6] Note, that these definitions require further elaboration. First, $\mathbf{p}_2$ is not always defined, since the Euler characteristic v_2 might become 0. Second, the definition of the half scale needs elaboration for cases, in which the curve under consideration crosses the zero line. The results that follow, however, do not depend on conventions for these cases.

In these terms, our measures are mainly responsive to “overall cell morphology” and “territorial coverage”. Our measures do not provide a reconstruction of hierarchical tree structures, as captured by measures of the fourth class in [2]. Note, in particular, that, different from a number of morphological descriptors such as Rall’s ratio, our approach is not based upon a prior division of a neuron into a number of elements like cylinders. No specific model assumptions are made. Our method is completely non-parametric.

Uylings and van Pelt [6] classified morphological measures as topological/metrical and “whole tree”/“within tree”. In these terms our approach is metrical in that the full spatial information is used (only the Euler characteristic is a topological invariant). Our approach is “whole tree” and even “whole cell”, since it takes information from all pixels of the cell image.

It is important to note that there are conceptual links between Minkowski valuations and some previously known measures. For instance, Minkowski valuations are related to differential geometry measures such as the curvature (see [14]). Differently from [14], however, we do not consider the curvature as a function of curve length, but rather integrate it over the whole boundary of the neuron image. Taking spatial moments of the curvature as we do for calculating $\mathbf{p}_2$ and $V_2^{j,k}$ reveals where the curvature is concentrated in a cell and how it is distributed.

A few other measures known from the specialized literature are embedded in our framework. The area and the perimeter often used in neurobiology are just two of the Minkowski functionals. We systematically extend these two quantities by considering the other Minkowski functionals and spatial moments, i.e. the Minkowski vectors and tensors. The center of mass (often called “the centroid”) is also part of our framework presented here. But there are a few other centroids as known in Integral Geometry. Our toy examples have shown how important the relative locations of all centroids are. It is particularly interesting that they express important information on the symmetry of a cell. In our framework it is straightforward to calculate the distance between the centroids and the soma centroid in order to quantify to what extent the soma is off-centered, which is a basic measure of symmetry.

For quantifying the asymmetry of neuronal cells, two-dimensional moments of inertia have been considered in the literature (see [6] and [38]). The moments of inertia are the eigenvalues of the inertial tensor and measure the principal dispersions of the area (see [42]). Our tensor $V_0^{2,0}$ has the same eigenvalues and eigenvectors as the inertia tensor. Our approach is to some extent more general than [6] since we also consider dilations of the cells with $r_s \neq 0$ and the other tensors such as $V_1^{1,0}$. These other tensors display the asymmetry of a cell with respect to other features (for instance, boundary length instead of area). We have also proposed to use Minkowski tensors for extracting different information such as the concentration of a cell by looking at the trace and comparing to scalar Minkowski functionals.

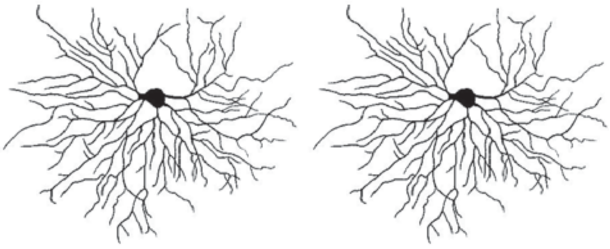
(a) (b)

Fig. 18. An illustration of the distortion we apply. (a): the original cell (α type); (b): a distortion of the cell in (a).

Table 2. The cell types and the numbers denoting the cells that were obtained from the cell types. For instance, the original α cell is labeled by 1; its four distortions are labeled by 2–5; and so forth.

Cell type	Nos.
α	1–5
β	6–10
δ	11–15
ϵ	16–20
η	21–25

Cell type	Nos.
ι	26–30
κ	31–35
λ	36–40
θ	41–45
ζ	46–50

A comparison to a Sholl analysis. In order to probe our method further, we compare it to a well-known approach, viz. a Sholl analysis. For each of our cells [27], we obtain a few distorted versions. The distorted cell images are produced by using a transformation tool implemented for “Gimp” [43]. Very roughly, the soma is shifted, and its former environment is warped so as to follow it. An example is shown in Figure 18. Although the distortions of the cells were obtained by hand, we did not tune them to any purpose.

We produce four distortions of each cell. In this way the shape space is populated with additional cells. Altogether we end up with 50 cells (10 original ones and 40 artifical ones). We number them consecutively: Cells 1–5 are the α cell and its distortions, and so on (see Tab. 2).

Our distortions reflect one special type of “morphological distortion”. It is therefore to be expected that, under some morphological characteristics, the distorted cells will be close to the originals ones, whereas, under different characteristics, they will not.

We can now compare our measurements to a Sholl analysis. We run a Sholl analysis over the 50 cells (see [6], p. 404 and references given therein). The number of branching points and the number of terminal points are recorded as functions of the distance from the soma. In order to obtain global measures for each individual cell, we calculate the mean and the standard deviation of both functions. The range of distances over which the branching/terminal points are recorded and averaged is the same for each cell. The Minkowski functionals and the higher-rank Minkowski valuations are also calculated and the global measures for each cell are obtained.

We then apply Ward’s hierarchical clustering method with Euclidean distances [44]. Results are presented in

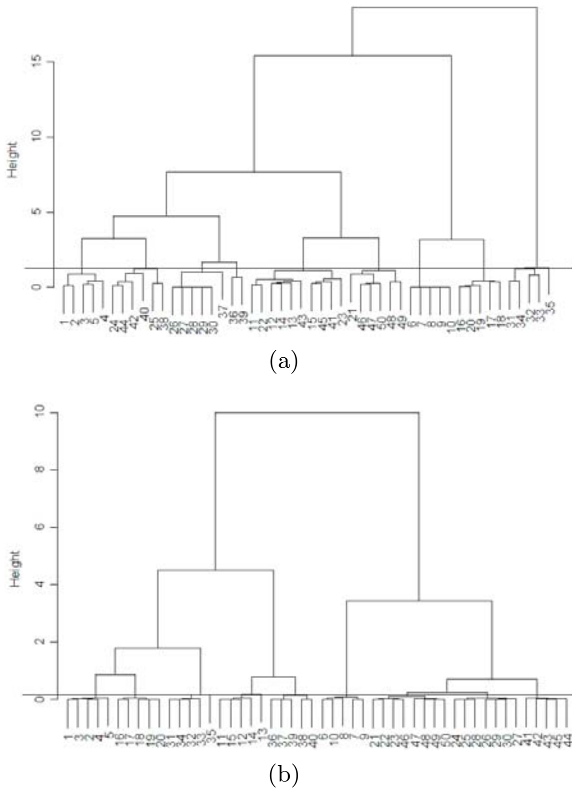

Fig. 19. Classification patterns according to an agglomerative hierarchical clustering analysis based upon (a) a Sholl analysis; (b) a variation of the isoperimetric ratio, Q.

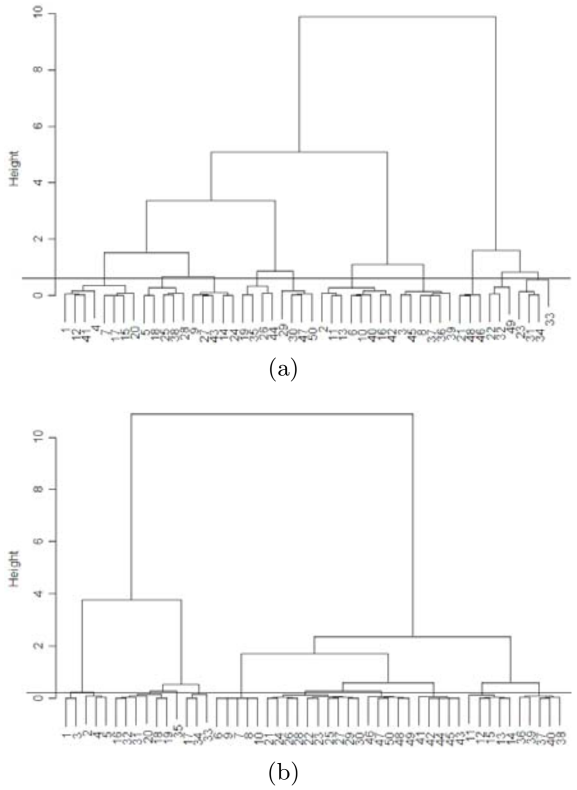

Fig. 20. Classification patterns according to an agglomerative hierarchical clustering analysis based upon (a) the anisotropy parameter $\overline{\mathrm{anis}}(V_1^{2,0})$ (b) a compacticity parameter defined in terms of $V_1^{2,0}$ and V_0.

Figures 19 and 20. The horizontal lines indicate the partition of the cells into 10 classes of neurons which we assume to exist. Each class is defined as the group of cells whose branching starts at the intersection with the horizontal line.

The top panel of Figure 19 shows a clustering diagram that was obtained on the base of the global parameters from the Sholl analysis. It shows that our "morphological distortion" changes the cell structure significantly, but that three of the original cells together with their distortions are regained as clusters.

The explanation is that our "morphological distortion" mostly leaves the numbers of arms and branching points invariant. However, since the soma is shifted, the distances of some branching points from the soma change. In this way there is some significant variation in cell structure which is reflected in the clustering diagram.

It is easy to regain a considerable fraction of the original cells together with their distortions as clusters in a dendrogram with Minkowski valuations as input. The reason is that the cells significantly differ in terms of size, which is not affected by our distortions, and some of the Minkowski functionals like V_0 or V_1 reflect the cell size. But we take it to be a trivial thing to distinguish the different cell types in terms of their size. So from now on, we will only look on dimensionless measures based upon the Minkowski valuations. They do not directly reflect size[7].

In the bottom panel of Figure 19 we show a clustering dendrogram that is based on the mean logarithm of Q. Very roughly, Q measures the excess perimeter given the area of a cell (see Eq. (4.12) for the definition). It only builds upon the scalar Minkowski functionals. It can be seen that six original cells and their distortions form clusters "in the right way". So in this regard, Q does better in grouping together the originals and their distortions than the Sholl analysis does. In order to understand why Q is such stable under our morphological distortions, look at the ϵ cell as an example. The ϵ cell displays a maximum value of Q because of its long, but isolated arms. The lengths and the separations of the arms are not much changed, if the soma is shifted.

The top panel of Figure 20 shows a clustering dendrogram that was obtained on the basis of the mean anisotropy from $V_1^{2,0}$, $\overline{\mathrm{anis}}(V_1^{2,0})$. The originals and their distortions are not at all grouped together in "the right way". But after a little reflection, this should not come as a surprise. The anisotropy parameters were obtained by calculating the tensor with the soma as center. If the soma

---

[7] We will not discuss to what extent the Sholl measure is affected by cell size.

is shifted, the whole cell is seen from a different perspective, and the anisotropy changes significantly.

The fact that the anisotropy parameter $\overline{\mathrm{anis}}(V_1^{2,0})$ does a worse job in regaining the original cells and their distortions, does not mean that higher-rank Minkowski valuations are useless. First, it is possible to form other dimensionless parameters on the basis of the valuations that do much better. For instance, we calculate $V_1^{2,0}$ with respect to $\mathbf{p}_1$ as origin, normalize its trace by $\sqrt{V_0}^3$, and take the mean. This yields another measure of how concentrated a cell is (similar measures were shown in Fig. 15; the new measure is somehow a "relative" of the isoperimetric ratio). If we apply the clustering algorithm for this measure, we get six cell types right. This is shown in the bottom panel of Figure 20. Second, quite to the contrary, there is a different way at looking at our dendrograms. The idea is that our measures provide different orderings of the cells according to different criteria. The fact that the anisotropy parameter generates a different dendrogram than the Q parameter shows that both measures highlight different aspects of morphology. They suggest a different taxonomy of the cells. This is also manifest from those parts of the dendrograms that lie above the horizontal line: they are different. We conclude that, altogether, there is a strong case for exploring the Minkowski functionals and higher-rank Minkowski valuations further.

5 Conclusions

The shape of a neuronal cell is an important indicator of its function. For instance, it has been suggested that the complexity and symmetry of the neuronal tree are associated with mental illnesses, see, e.g. [45]. For this reason, the characterization of neuronal anatomy is a thriving field of research, see, for instance, [6,14] and references therein. The stages of the growth of neurons [45] as well as the morphology of their mature form [6] are frequently investigated, particularly with an eye to clues about abnormalities caused by malformations or diseases. In both cases there is a need for objective and quantitative measures in order to account for the variety of morphological features found in neuronal cells.

In this work we have advanced recent work on Minkowski functionals [18,19], which proposed a framework to characterize the morphology of neurons using simple algorithms based on integral geometry. We have described an extension of the scalar Minkowski *functionals* to higher-rank Minkowski *valuations*. These valuations have been successfully explored elsewhere [26] and suggest themselves as an effective tool for characterizing point distributions. Whereas the scalar functionals are invariant under motions in Euclidean space, the higher-rank valuations trade invariance for sensitivity to cell symmetry.

We have first performed a multi-scale analysis on the base of the higher-rank Minkowski valuations, i.e. we showed the valuations or some simple functions of them such as the asymmetry as a function of dilation scale. We have then suggested several ways to obtain global measures that integrate information from all scales. As far as our limited set of cells is concerned, we could find significant differences (as well as similarities) between the prototypes for each category of cells. Note that the very definitions of those classes are based upon physiological, classical geometric measurements and take into account the localization in the tissue of the cell sample. On the contrary, our measures are purely geometric and do not take into account the cells' localizations.

We have also carried out a comparison between the traditional Sholl analysis, the scalar Minkowski functionals and the new, extended framework presented in this paper. For each prototype cell, we have produced a set of four distorted images (for details see above). We have then analyzed these images with the different methods and thus obtained several morphometric descriptions of the cells. Each morphometric description has been subject to a Ward's clustering algorithm. The dendrograms obtained in this way (see Figs. 19 and 20) show the robustness of some of our new measures, as far as a special type of morphological distortion is concerned. We found some measures based upon the scalar Minkowski functionals only, and based upon the Minkowski valuations more broadly, that do a better job in regaining the original cell with their distortions than the Sholl analysis does. The dendrograms obtained also suggest different taxonomies of the cell types. This indicates that the higher-rank Minkowski valuations provide a complementary perspective on the cells. It is still open, however, whether the differences found between the prototypes will be characteristic of all ganglionary neurons in a statistical sense and whether the taxonomies will prove stable for larger data sets.

Altogether, the comparison to other approaches shows that Minkowski valuations provide a framework for embedding and systematically extending measures previously known. Due to their axiomatic characterization, Minkowski valuations display information *that is complete in a specific and well-defined way.* Therefore, Minkowski valuations suggest a natural way of extending previously known characteristics. By embedding these characteristics in integral geometry we also deepen our general understanding of morphometry. Methods from integral geometry might even help to find more efficient algorithms for calculating previously known measures. Altogether Minkowski valuations significantly enrich our tool-box for neuromorphometry in two and three dimensions.

This work was financially supported by FAPESP (processes 02/02504-01 and 99/12765-2) and CNPq (process 308231/03-1). It was also supported by the "Sonderforschungsbereich 375-95 für Astro-Teilchenphysik" der Deutschen Forschungsgemeinschaft. C.B. thanks the Alexander von Humboldt Foundation, the German Federal Ministry of Education and Research and the Program for the Investment in the Future (ZIP) of the German Government for supporting this research. He also thanks Jens Schmalzing for providing software on which parts of the codes for this paper are built upon. We finally thank Fionn Murtagh for providing clustering software that was used in our work.

References

1. S. Douady, Y. Coulder, Phys. Rev. Lett. **68**, 2098 (1992)
2. L. da F. Costa, E.T.M. Manoel, Neuroinformatics **1**, 65 (2003)
3. H. Wässle, B.B. Boycott, R.B. Illing, Phil. Trans. R. Soc. **212**, 177 (1981)
4. Y. Fukuda, C.F. Hsiao, M. Watanabe, H. Ito, J. Neurophysiol. **52**, 999 (1984)
5. A. van Ooyen, J. Duijnhouwer, M.W.H. Remme, J. van Pelt, Network: Comput. Neural Syst. **13**, 311 (2002)
6. H.B.M. Uylings, J. van Pelt, Network: Comput. Neural Syst. **13**, 397 (2002)
7. L. da F. Costa, T.J. Velte, Journal of Comparative Neurology **404**, 33 (1999)
8. G.A. Ascoli, J.L. Krichmar, Neurocomputing **48**, 1003 (2000)
9. R.C. Coelho, L. da F. Costa, Neurocomputing **48**, 555 (2001)
10. S. Peng, B. Urbanc, L. Cruz, B.T. Hyman, H.E. Stanley, Proc. Nat. Ac. Sci. **100**, 3847 (2003)
11. F. Rieke, D. Warland, R. de Ruyyter van Steveninck, W. Bialek, *Spikes: Exploring the Neural Code* (Bradford Books, 1999)
12. K. Morigiwa, M. Tauchi, Y. Fukuda, Neurosci. Res. **10**, S131 (1989)
13. R.C. Coelho, L. da F. Costa, Applied Signal Processing **3**, 163 (1996)
14. L. da F Costa, E.T.M. Manoel, F. Faucereau, J. Chelly, J. van Pelt, G. Ramakers, Network: Comput. Neural Syst. **13**, 283 (2002)
15. T.G. Smith, G.D. Lange, W.B. Marks, J. Neuroci. Methods **69**, 133 (1996)
16. E.P. Rodrigues, M.S. Barbosa, L. da F. Costa, Phys. Rev. E (2004)
17. R.M. Cesar, L. da F. Costa, Biological Cybernetics **79**, 347 (1998)
18. M.S. Barbosa, E.S. Bernardes, L. da F. Costa, Phys. Rev. E **67** (2003)
19. M.S. Barbosa, L. da F. Costa et al., Eur. Phys. J. B **37**, 109 (2003)
20. P. Soille, *Morphological Image Analysis. Principles and Applications* (Springer, Berlin, 1999)
21. K. Michelsen, H. de Raedt, Phys. Rep. **347**, 461 (2001)
22. S. Alesker, Geom. Dedicata **74**, 241 (1999)
23. R. Schneider, Rend. Circ. Mat. Ser II, Suppl. **65**, 355 (2000)
24. R. Schneider, R. Schuster, Rend. Circ. Mat. Ser II, Suppl. **70**, 295 (2002)
25. C. Beisbart, R. Dahlke, K. Mecke, H. Wagner, in *Morphology of Condensed Matter. Physics and Geometry of Spatial Complex Systems*, edited by K. Mecke, D. Stoyan (Springer, 2002), Vol. 600 of *Lecture Notes in Physics*, pp. 238–260, `arXiv:physics/0203072`
26. C. Beisbart, T. Buchert, H. Wagner, Physica A **293**, 592 (2001)
27. R.H. Masland, Nature Neuroscience **4**, 877 (2001)
28. B.J. O'Brien, T. Isayama, R. Richardson, D.M. Berson, J. Phys. **538.3**, 787 (2002)
29. H. Hadwiger, *Vorlesungen über Inhalt, Oberfläche und Isoperimetrie* (Springer Verlag, Berlin, 1957)
30. W. Weil, in *Convexity and its Applications*, edited by P.M. Gruber, J.M. Wills (Birkhäuser, Basel, 1983), pp. 360–412
31. S. Alesker, Ann. of Math. **149**, 977 (1999)
32. H. Hadwiger, C. Meier, Mathematische Nachrichten **56**, 361 (1974)
33. C. Beisbart, K. Mecke, unpublished Manuscript 2005
34. C. Beisbart, Ph.D. thesis, Ludwig–Maximilians–Universität München (2001), `http://edoc.ub.uni-muenchen.de/archive/00000483/01/Beisbart_Claus.pdf`
35. K. Mecke, T. Buchert, H. Wagner, Astronomy and Astrophysics **288**, 697 (1994)
36. M. Pu, D.M. Berson, T. Pan, The journal of Neuroscience **14** (1994)
37. D.M. Berson, M. Pu, E.V. Famiglietti, Journal of Comparative Neurology **399**, 269 (1998)
38. R.C.C. et al., Real-Time Imaging **8**, 213 (2002)
39. D. Fenchel, C.R. Acad. Sci. Paris **203**, 647 (1936), in French
40. A.D. Alexandrov, Matem. Sb. SSSR **2**, 1205 (1937), in Russian, summary in German
41. J. Schmalzing, T. Buchert, A.L. Melott, V. Sahni, B.S. Sathyaprakash, S.F. Shandarin, ApJ **526**, 568 (1999)
42. L. da F. Costa, R.M.C. Jr., *Shape Analysis and Classification: Theory and Practice* (CRC, 2000)
43. N. Schmitz, *Iwarp: Gimp Plugin*, `www.gimp.org`
44. J.H. Ward, J. Am. Stat. Ass. **58**, 236 (1963)
45. K.L. Whitford, P. Dijkhuizen, F. Polleux, A. Ghosh, Annu. Rev. Neurosci. **25**, 127 (2002)